Fabrication of Magnetically Recoverable Catalysts Based on Mixtures of Pd and Iron Oxide Nanoparticles for Hydrogenation of Alkyne Alcohols

Rosemary Easterday,[†,⊥] Clara Leonard,[†] Olivia Sanchez-Felix,[†] Yaroslav Losovyj,[†] Maren Pink,[†] Barry D. Stein,[‡] David Gene Morgan,[†] Nadezhda A. Lyubimova,[§] Linda Zh. Nikoshvili,[§] Esther M. Sulman,[§] Waleed E. Mahmoud,[‖] Ahmed A. Al-Ghamdi,[‖] and Lyudmila M. Bronstein*[†,‖]

[†]Department of Chemistry, Indiana University, 800 E. Kirkwood Avenue, Bloomington, Indiana 47405, United States,
[‡]Department of Biology, Indiana University, 1001 East Third Street, Bloomington, Indiana 47405, United States
[§]Department of Biotechnology and Chemistry, Tver State Technical University, 22 A. Nikitina St, 170026 Tver, Russia
[‖]Department of Physics, Faculty of Science, King Abdulaziz University, Jeddah, Saudi Arabia

Ⓢ *Supporting Information*

ABSTRACT: We report a novel method for development of magnetically recoverable catalysts prepared by thermal decomposition of palladium acetylacetonate in the presence of iron oxide nanoparticles (NPs). Depending on conditions, the reaction results either in a dispersed mixture of Pd and iron oxide NPs or in their aggregates. It was demonstrated that the Pd loading, reaction temperature, solvent, and iron oxide NP size and composition are crucial to control the reaction product including the degree of aggregation of Pd and iron oxide NPs, and the catalyst properties. The aggregation controlled by polarization and magnetic forces allows faster magnetic separation, yet the aggregate sizes do not exceed a few hundred nanometers, making them suitable for various catalytic applications. These NP mixtures were studied in a selective hydrogenation of 2-methyl-3-butyn-2-ol to 2-methyl-3-buten-2-ol, demonstrating clear differences in catalytic behavior depending on the catalyst structure. In addition, one of the catalysts was also tested in hydrogenation of 3-methyl-1-pentyn-3-ol and 3-methyl-1-nonyn-3-ol, indicating some specificity of the catalyst toward different alkyne alcohols.

KEYWORDS: magnetically recoverable catalysts, palladium nanoparticles, iron oxide nanoparticles, hydrogenation
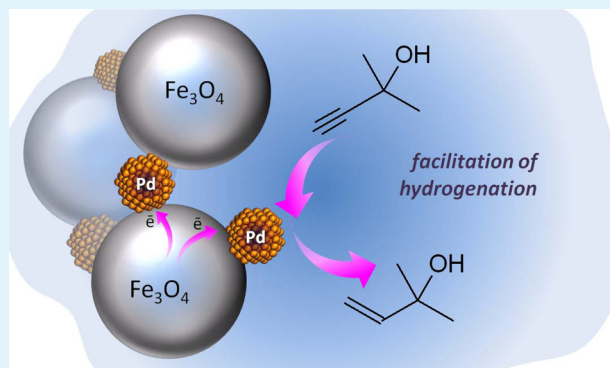
■ INTRODUCTION

Palladium nanoparticles (NPs) are widely used in the selective hydrogenation of alkynes due to their high selectivity in such processes.[1−4] Recently, Pd-containing magnetically recoverable catalysts received considerable attention due to facile catalyst recovery,[2,5−11] environmentally friendly processes, and less expensive target products.[12−18]

In this paper we report a novel method for development of magnetically recoverable catalysts based on palladium and iron oxide nanoparticles. Previously, our group reported formation of PtFe NPs by thermal decomposition of Pt acetylacetonate, Pt(acac)₂, in the presence of maghemite NPs.[19] It was demonstrated that the existence of iron oxide NPs in a catalytic mixture with PtFe NPs improves the catalyst performance. In the present work Pd(acac)₂ is used as a Pd source, and well-defined iron oxide NPs of different compositions serve as an iron source. Depending on the conditions, the reaction results either in a dispersed mixture of Pd and iron oxide NPs or in their aggregates. The latter allow

faster magnetic separation, yet the aggregate sizes do not exceed a few hundred nanometers, thus making them suitable for various catalytic applications including those in microreactors. These NP mixtures were studied in the selective hydrogenation of 2-methyl-3-butyn-2-ol (MBY) to 2-methyl-3-buten-2-ol (MBE), demonstrating clear differences in catalytic behavior depending on the catalyst structure. It is noteworthy that MBE has also a commercial value as an intermediate for fragrant substances and vitamins E and K.[20] In addition, one of the catalysts was also tested in the hydrogenation of 3-methyl-1-pentyn-3-ol (MPY) and 3-methyl-1-nonyn-3-ol (MNY) to assess specificity of the catalyst toward different alkyne alcohols.

In this paper we demonstrate that the Pd loading, reaction temperature, solvent, and iron oxide NP size and composition are key parameters to control the reaction product, the degree

Table 1. Reaction Conditions for the Formation of Pd−Iron Oxide NP Containing Samples

sample notation	iron oxide NP type	iron oxide NP size, nm	standard deviation, %	Pd(acac)$_2$ amount, mg	solvent	reaction temperature, °C	yield, %	Pd NP size, nm	standard deviation, %
Pd-1	Fe$_3$O$_4$/γ-Fe$_2$O$_3$	8.3	7.6	0.025	dioctyl ether	285	75.1	6.7	22.0
Pd-2	Fe$_3$O$_4$/γ-Fe$_2$O$_3$	8.3	7.6	0.0125	dioctyl ether	285	71.9	5.9	17.7
Pd-3	Fe$_3$O$_4$/γ-Fe$_2$O$_3$	8.3	7.6	0.00625	dioctyl ether	285	72.4	6.2	22.3
Pd-4	Fe$_3$O$_4$/γ-Fe$_2$O$_3$	8.3	7.6	0.025	diphenyl ether	250	68.3	5.9	17.6
Pd-5	Fe$_3$O$_4$/γ-Fe$_2$O$_3$	8.3	7.6	0.025	diphenyl ether	200	62.2	5.9	18.7
Pd-6	Fe$_3$O$_4$/γ-Fe$_2$O$_3$	8.3	7.6	0.025	dioctyl ether	200	79.1	5.6	22.8
Pd-7	none			0.025	dioctyl ether	285	81.2	6.4	58.0
Pd-8	Fe$_3$O$_4$/γ-Fe$_2$O$_3$	22.8	12.3	0.025	diphenyl ether	250	67.8	6.2	37.1
Pd-9	Fe$_3$O$_4$/γ-Fe$_2$O$_3$	22.8	12.3	0.025	dioctyl ether	285	77.3	4.3	41.1
Pd-10	FeO−Fe$_3$O$_4$	22.6	11.7	0.025	diphenyl ether	250	72.3	6.0	20.3

of aggregation of Pd and iron oxide NPs, and the catalyst properties. To assess the influence of the catalyst structure and morphology on its properties, the NP mixtures were characterized using transmission electron microscopy (TEM), X-ray powder diffraction (XRD), dynamic light scattering (DLS), X-ray photoelectron spectroscopy (XPS), and energy-dispersive X-ray spectroscopy (EDS).

■ EXPERIMENTAL SECTION

Materials. FeCl$_3$·6H$_2$O (98%), decane (≥99%), octadecane (99%), eicosane (99%), dioctyl ether (99%), toluene (99.8%), diphenyl ether (≥98%), 1,2-hexadecane diol (90%), oleylamine (OAm, 70%), oleic acid (OA, 90%), Pd(acac)$_2$ (97%), and MBY (≥98%) were purchased from Sigma-Aldrich and used as-received. MPY (97%) and MNY (97%) were purchased from Alfa Aesar and used as-received. Hexanes (85%), ethanol (95%), and acetone (99.78%) were purchased from EMD Chemicals and used without purification. Chloroform (Mallinckrodt, 100%) was also used as received.

Synthetic Procedures. *Iron Oxide Nanoparticle Synthesis.* Iron oleate was synthesized according to a published procedure.[21] Iron oxide NPs were synthesized via the thermal decomposition of iron oleate using procedures published elsewhere.[22,23] The NPs were prepared in octadecane and eicosane as solvents, which were chosen to control the reaction temperature and achieve the desired NP size. The resultant NPs were stored as a solid reaction solution (as octadecane and eicosane are solid at room temperature) and refrigerated until needed. Oxidation of as-synthesized NPs was carried out according to the procedure described elsewhere.[19,23]

Synthesis of Pd/Iron Oxide NPs. In a typical procedure, chloroform was evaporated in vacuum from a solution containing 15 mg of iron oxide NPs. Then the NPs were dispersed in 7 mL of dioctyl ether and sonicated for 20 min. A three-neck round-bottom flask was charged with 0.05 g of 1,2-hexadecane diol, 10 μL of OAm, 10 μL of OA (both OAm and OA used as surfactants), and the NP solution. The flask was equipped with a reflux condenser, temperature probe, argon inlet, and a stir bar. Argon was bubbled into the solution via a needle for 15 min. The solution was then heated at 10 °C/min to 285 °C. Once the solution reached 285 °C, a suspension of 0.025 g of Pd(acac)$_2$ in 0.25 mL of dioctyl ether was injected into the reaction solution and the latter was maintained at 285 °C for 45 min. The solution was then cooled and transferred to a vial. The sample was stored in a refrigerator. The reaction conditions and the characteristics of the samples are presented in Table 1.

Characterization. Electron-transparent NP specimens for TEM were prepared by placing a drop of a diluted solution onto a carbon-coated Cu grid. Images were acquired at an accelerating voltage of 80 kV on a JEOL JEM1010 transmission electron microscope. Images were analyzed with the National Institute of Health developed image-processing package ImageJ to estimate NP diameters. Between 150 and 300 NPs were used for this analysis. High-resolution TEM (HRTEM) images and scanning TEM (STEM) EDS were acquired at an accelerating voltage of 300 kV on a JEOL 3200FS transmission electron microscope equipped with an Oxford Instruments INCA EDS system. The same TEM grids were used for all analyses.

XRD patterns were collected on an Empyrean from PANalytical. X-rays were generated from a copper target with a scattering wavelength of 1.54 Å. The step size of the experiment was 0.02.

DLS measurements were performed using a Malvern Zetasizer Nano ZS. Measurement duration was set to be determined automatically, and data were averaged from at least three runs. Intensity distributions of the particle sizes were recorded.

XPS experiments were performed using PHI Versa Probe II instrument equipped with a monochromatic Al Kα source. The X-ray power of 25 W at 15 kV was used for a 100 μm beam size. The instrument work function was calibrated to give a binding energy (BE) of 84.0 eV for the Au 4f$_{7/2}$ line for metallic gold and the spectrometer dispersion was adjusted to give BEs of 284.8, 932.7, and 368.3 eV for the C 1s line of adventitious (aliphatic) carbon present on the nonsputtered samples, and Cu 2p$_{3/2}$ and Ag 3d$_{5/2}$ photoemission lines, respectively. The PHI double-charge compensation system was used on all samples. The ultimate Versa Probe II instrumental resolution was determined to be better than 0.125 eV using the Fermi edge of the valence band for metallic silver. XPS spectra with the energy step of 0.1 eV were recorded using SmartSoft-XPS v2.0 and processed with PHI MultiPack v9.0 and/or CasaXPS v.2.3.14 at pass energies of 23.5 and 11.75 eV for Fe 2p and Pd 3d (both C 1s) and O 1s regions, respectively. Peaks were fitted using GL line shapes and/or asymmetric shapes, that is, a combination of Gaussians and Lorentzians with 10−50% of Lorentzian contents. Shirley background was used for curve fitting. NP samples for XPS were prepared by drop casting from solution onto the native surface of a Si(111) wafer.

Catalytic Studies. Catalytic testing was carried out in a 60 mL isothermal glass batch reactor installed in a shaker and connected to a gasometric buret (for hydrogen consumption control). The volume of the hydrogen consumed was in the range of 535−810 mL (depending on the amount of the alkyne alcohol used) that was close to the stoichiometric amount for each experiment. Toluene was chosen as a solvent because of the highest affinity toward the catalyst (close to that of chloroform), allowing a good catalyst dispersion. The total volume of the liquid phase (including toluene and an alkyne alcohol) was 30 mL. In each experiment the amount of MBY was varied from 2 g (23.8

mmol) up to 3 g (35.7 mmol), while the catalyst amount was in the range of 0.3−2 mg (depending on the Pd content in the catalyst) to provide the MBY-to-Pd molar ratio of about 10 000. In the case of MPY and MNY, the same substrate-to-Pd molar ratios have been used. Reaction conditions were ambient hydrogen pressure, stirring rate of 850 shakings per minute, and temperature of 90 °C.

Samples were periodically taken and analyzed via gas chromatography-mass spectrometry (Shimadzu GCMS-QP2010S) equipped with a capillary column HP-1MS (30 m × 0.25 mm i.d., 0.25 μm film thickness). Helium was used as a carrier gas at a flow rate of 1 mL/min. Analysis conditions: oven temperature 60 °C (isothermal), injector and interface temperature 280 °C, ion source temperature 260 °C, range from 10 up to 200 m/z. Decane was used as an internal standard with a concentration of 0.005 mol/L in the toluene solution. Retention times were the following: 1.53 min for MBY, 1.57 min for MBE, 1.70 min for MBA, 2.16 min for MPY, 2.25 min for MPE, 2.56 min for MPA, 4.57 for MNY, 4.86 for MNE, 5.62 for MNA, and 11.07 min for decane. The concentrations of the reaction mixture components Y_i were calculated from the corresponding calibration curves. Conversion was defined as

$$X = (Y_{S0} - Y_S)/Y_{S0} \times 100\%$$

where Y_{S0} is the initial substrate concentration and Y_S is the substrate concentration in the analyzed sample of the reaction mixture. Selectivity to target product (P) was defined as

$$S_P = Y_P/(Y_{S0} - Y_S) \times 100\%$$

For catalyst recycling, the catalyst was separated using a rare earth magnet, washed with toluene and chloroform, and dried at 70 °C for 3 h. Before reuse in the hydrogenation reaction, the catalyst was sonicated for 10 min in 2 mL of toluene. The brief sonication was a precaution to make sure that the aggregation due to magnetic separation did not change the catalyst properties.

■ RESULTS AND DISCUSSION

Initial Iron Oxide NPs. The majority of iron oxide NPs used in this work were additionally oxidized by heating a reaction solution of as-synthesized iron oxide NPs (prepared by thermal decomposition of iron oleate[22]) for 2 h at 200 °C in air.[19,23] Figure 1 shows a typical NP sample before and after
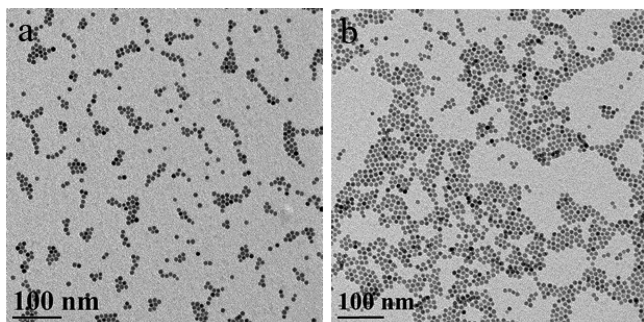

Figure 1. Iron oxide NPs before (a) and after (b) oxidation. The diameter of as-synthesized FeO−Fe$_3$O$_4$ NPs (a) is 8.1 nm with the 8.0% standard deviation. For oxidized Fe$_3$O$_4$/γ-Fe$_2$O$_3$ NPs (b), the diameter is 8.3 nm with the 7.6% standard deviation.

oxidation, indicating that additional oxidation has nearly no influence on the NP size and morphology. In our preceding papers, it was determined that the NPs before oxidation consist of two phases, FeO and Fe$_3$O$_4$, with the former phase prevailing, while after oxidation the NPs consists of either Fe$_3$O$_4$ or γ-Fe$_2$O$_3$.[22,23] Recent XPS studies of oxidized NPs demonstrated that they have the Fe$_3$O$_4$/γ-Fe$_2$O$_3$ structure with

approximately 15% of Fe^{2+} species, that is, with a Fe^{2+}/Fe^{3+} ratio of 0.18.[24] This matches 54% of the Fe$_3$O$_4$ phase.

To assess the electronic structure of these NPs (i.e., the surface versus bulk morphology), we have performed angular-dependent high-resolution XPS [Figure S1, Supporting Information (SI)]. No significant differences were observed in the spectra obtained at different experimental geometries, suggesting a high level of uniformity across the NPs and most probably the absence of a core−shell structure. Sputtering experiments have been also performed using 2 min cycles of 0.5 kV Ar ion beam. No significant changes were observed up to two sputtering cycles (Figure S2, SI), suggesting stability of the iron oxide NP structure. Further sputtering (3−4 cycles, not shown here) resulted in the reduction of iron species.

Structure of the Mixed NP Sample. For the Pd NP syntheses in the presence of iron oxide NPs, dioctyl ether was chosen because it is a good solvent for iron oxide NPs coated with OA and the resultant Pd (or PdFe) NPs stabilized with OA and OAm. In addition, it allows for a high reaction temperature (285 °C), which is beneficial for fast decomposition of Pd(acac)$_2$. Figure 2a shows the TEM image of Pd
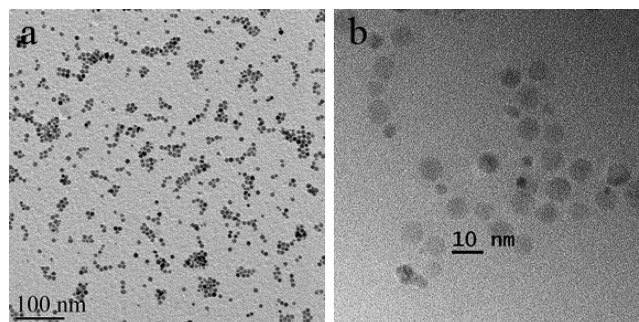

Figure 2. TEM (a) and HRTEM (b) images of Pd-1 prepared with 0.025 g of Pd(acac)$_2$.

NPs prepared in the presence of the 8.3 nm Fe$_3$O$_4$/γ-Fe$_2$O$_3$ NPs. The sample consists of two types of particles whose sizes and appearance differ. To evaluate the composition of both kinds of NPs, the Pd-1 sample (Table 1) was examined using HRTEM (Figure 2b) and EDS (Figure 3). Figure 2b shows that a spacing between lattice fringes in slightly larger particles is 2.46 Å which corresponds to the distance between the (311) planes in Fe$_3$O$_4$ (or spinel).[25,26] The lattice fringe spacing in smaller NPs is 2.22 Å which is close to the lattice spacing of the (111) planes of the fcc palladium (0.223 nm).[27] Figure 3 presents a STEM dark-field image and STEM EDS Fe and Pd maps of Pd-1. Two types of NPs are clearly seen in both the dark-field image (NPs with different electron densities) and the corresponding maps. Pd NPs do not contain iron, while iron oxide NPs are not coated by Pd.

A survey XPS spectrum of Pd-1 displayed in Figure S3 (SI) shows the presence of Pd, Fe, C, O, and Si. Si comes from the silicon wafer. The high-resolution XPS spectra of Pd-1 in the Fe 2p, O 1s, and the Pd 3d regions are presented in Figure 4. This figure also shows the XPS spectra of the initial iron oxide NPs (for Fe 2p and O 1s) used in the reaction. Only negligible differences were observed in the Fe 2p region (Figure 4a), mostly seen at the high binding energy part of the spectra. Binding energies for the iron species in both samples are about 710.8 eV, which is consistent with previous reports.[24,28−30] Similarly, the oxygen 1s region shows almost identical spectra
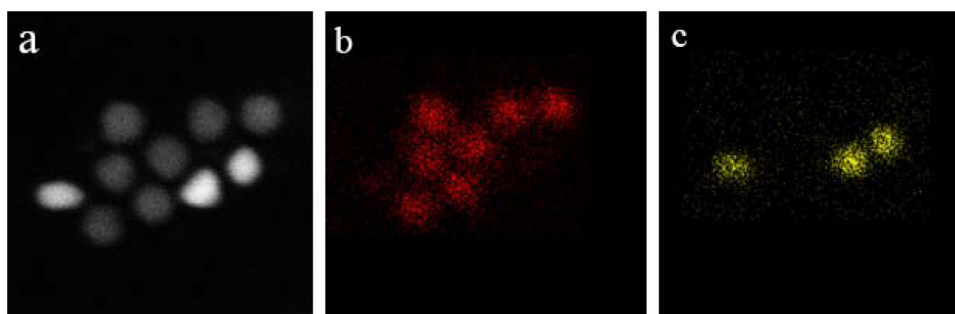
21654

dx.doi.org/10.1021/am5067223 | ACS Appl. Mater. Interfaces 2014, 6, 21652−21660

Figure 3. STEM dark-field image (a) and Fe (b) and Pd (c) EDS maps of Pd-1.
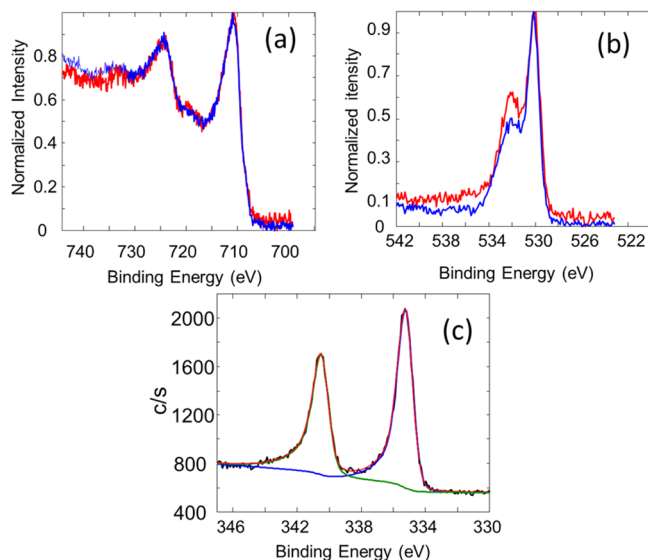

Figure 4. High-resolution XPS spectra of Pd-1 (red) and initial iron oxide NPs (blue) in the Fe 2p (a) and O 1s (b) regions. (c) High-resolution Pd 3d XPS spectrum of Pd-1; the black line represents experimental data, while the red line shows a generated fit (see Table S1, SI, for fitting parameters).

Figure 5. XRD pattern of Pd-1.

(Figure 4b) with the same binding energies. These data indicate that the iron oxide NPs do not change in the reaction conditions. The deconvolution of the XPS spectrum of Pd-1 in the Pd 3d region (Figure 4c) shows a Pd $3d_{5/2}$ binding energy of 335.2 eV, which is consistent with the Pd species in a metallic form (Pd^0).[31−33] Sputtering experiments showed no significant changes in the Pd 3d, Fe 2p, and O 1s regions (Figure S4, SI), which suggests a robust structure of the Pd/iron oxide NP mixture upon argon ion bombardment.

The XRD pattern of Pd-1 presented in Figure 5 also confirms the mixed character of the sample. Three reflections in the XRD pattern at 2θ = 40°, 46°, and 68° are attributed to the (111), (200), and (220) planes of a face-centered cubic (fcc) crystal structure of palladium.[27] The reflections at 2θ = 30.3°, 35.6°, 43.3°, 54.0°, 57.2°, and 62.9° correspond to the (220), (311), (400), (422), (511), and (440) crystallographic planes of a spinel phase (magnetite or maghemite), respectively.[34,35]

Influence of the Pd Precursor Amount, Reaction Temperature, Size, and Type of Iron Oxide NPs. A decrease of the Pd(acac)$_2$ loading from 0.025 to 0.0125 g and then to 0.0063 g (Table 1) leads to similar samples (Figure S5, SI) but with fewer Pd NPs. To assess the influence of iron oxide NPs on the Pd NP formation, a reference sample was prepared with 0.025 g of Pd(acac)$_2$ in the absence of Fe$_3$O$_4$/γ-
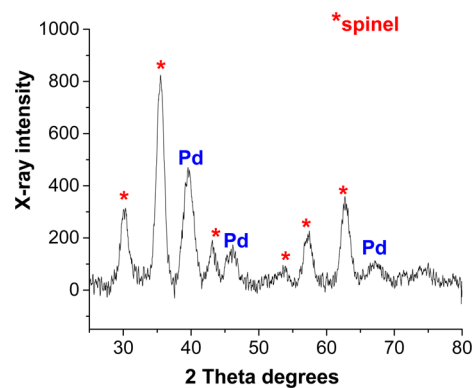
Fe$_2$O$_3$ NPs but otherwise identical conditions (Figure S5c, SI). In the reference sample Pd NPs are not stabilized and fully aggregated, revealing a stabilizing influence of iron oxide NPs. A similar stabilizing influence was reported earlier in the case of Pt-containing samples.[19]

Because our goal was a controlled formation of the aggregates of Pd and iron oxide NPs for easier magnetic separation, we also used diphenyl ether as solvent because it has lower affinity toward the above NPs, thus, possibly promoting aggregation. The use of diphenyl ether results in a lower reaction temperature (250 °C) because its boiling point is 259 °C. Indeed, the reaction product obtained in such conditions (Pd-4, Table 1) contained some aggregates of Fe$_3$O$_4$/γ-Fe$_2$O$_3$ NPs that trapped small Pd NPs (Figure 6a) as was confirmed by DLS data (Figure S6a, SI). It is noteworthy that a decrease of the reaction temperature to 200 °C resulted in much larger and denser aggregates (Figure 6b and Figure S6a, SI). Attachment of Pd NPs to the iron oxide NPs suggests that at 200 °C in diphenyl ether a Pd NP formation might occur
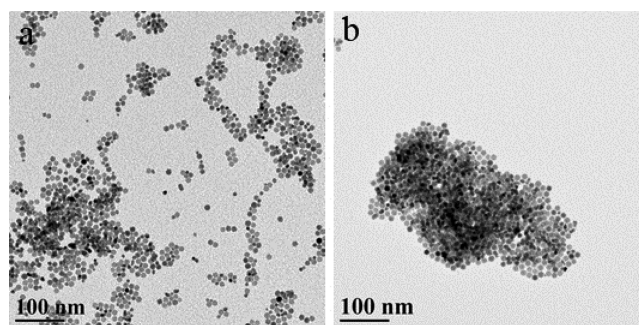

Figure 6. TEM images of Pd-4 (a) prepared at 250 °C and Pd-5 (b) prepared at 200 °C in diphenyl ether.
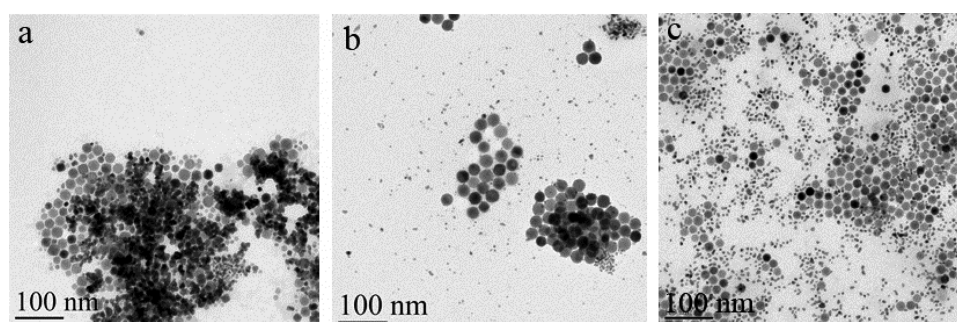
Figure 7. TEM images of Pd-8 (a), Pd-9 (b), and Pd-10 (c).

heterogeneously on the iron oxide NP surface, while in boiling dioctyl ether rather homogeneous nucleation takes place. It is noteworthy that the Pd-6 sample (Table 1) prepared at 200 °C in dioctyl ether was equally aggregated (not shown), indicating that the reaction temperature has a stronger influence on aggregation than the type of solvent.

The use of larger iron oxide NPs, 22.8 nm, instead of 8.3 or 11.0 nm, results in more pronounced NP aggregation in the reaction product obtained at 250 °C in diphenyl ether as is seen from the comparison of Figures 6a and 7a displaying TEM images of Pd-4 and Pd-8, respectively (Table 1). The larger aggregation in the Pd-8 sample is also confirmed by DLS data (Figure S6, SI). Moreover, for 22.8 nm iron oxide NPs, even the reaction at 285 °C in dioctyl ether results in partial aggregation, indicating stronger magnetic attraction of larger iron oxide NPs (Figure 7b). The replacement of oxidized Fe_3O_4/γ-Fe_2O_3 NPs with as-synthesized FeO-Fe_3O_4 NPs of the same size (Pd-10, Figure 7c) leads to decreased aggregation, which could be assigned to weaker magnetic interactions of as-synthesized FeO-Fe_3O_4 NPs as was observed during magnetic separation. The HRTEM and dark-field STEM images of Pd-10 are shown in Figure 8. The Pd NPs are represented by nearly
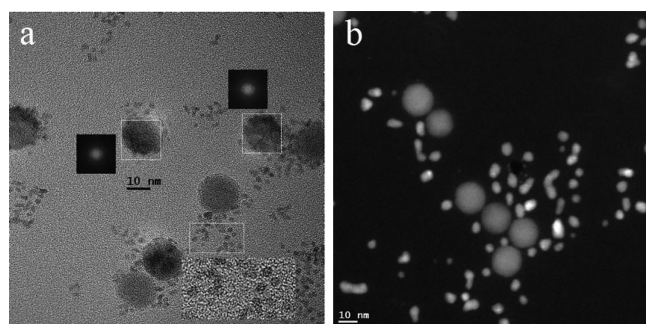

Figure 8. HRTEM (a) and dark-field STEM image (b) of Pd-10. Insets in (a) show fast Fourier transform (FFT) patterns (dark) and a higher magnification image of small particles (lower right). Brighter, smaller NPs in (b) are Pd NPs, while larger and darker NPs consist of iron oxide.

spherical particles and also fused particles consisting of two or three single particles. It is worth noting that, for all the samples, the Pd NP diameters are about 6 nm and hardly depend on the reactions conditions.

The HRTEM image and the FFT patterns of Pd-10 (Figure 8a) indicate, however, that the iron oxide NPs are single crystals with similar spacing as those found for the Pd-1 sample (Figure 2). Since the initial iron oxide NPs in this case were

FeO−Fe_3O_4, additional oxidation may occur with OA and/or acetylacetone during Pd NP formation.

High-resolution XPS spectra of Pd-10 in the Fe 2p, O 1s, and Pd 3d regions are presented in Figure 9. The satellite structure
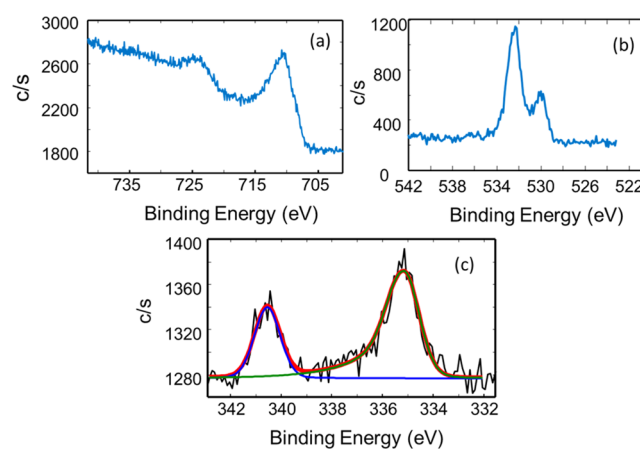

Figure 9. High-resolution (a) Fe 2p, (b) O 1s, and (c) Pd 3d XPS spectra of Pd-10. See Table S2 (SI) for Pd 3d deconvolution parameters.

at about 719.5 eV BE in the Fe $2p_{3/2}$ region is nearly absent. The lack of this feature along with a Fe^{2+}/Fe^{3+} ratio of 0.47 (obtained from the Fe 3p region, Figure S7, SI) are consistent with bulk Fe_3O_4 (Fe^{2+}/Fe^{3+} = 0.5). Similar to Pd-1, the deconvolution of the XPS spectrum of Pd-10 in the Pd 3d region (Figure 9c and Table S2, SI) gives a Pd $3d_{5/2}$ binding energy of 335.12 eV, which matches that of Pd^0.[31−33]

Aggregation Mechanism of Pd and Fe_3O_4/γ-Fe_2O_3 NPs. To better understand the aggregation mechanism of iron oxide and Pd NPs, we carried out a synthesis at 200 °C in diphenyl ether (Pd-5, Table 1), taking specimens of the reaction solution 5, 15, and 25 min after the injection of the $Pd(acac)_2$ solution. Already 5 min after the $Pd(acac)_2$ injection some aggregation occurs although Pd NPs exist both on the surface of iron oxide NPs and in solution, while $Pd(acac)_2$ is not fully decomposed (gray matter in the background indicated by a red arrow) (Figure S8a, SI). In the specimen taken out after 15 min, all iron oxide and Pd NPs are aggregated and no precursor is visible in the background (Figure S8b, SI). No changes were observed in the reaction product isolated after 25 min (Figure S8c, SI). Thus, the following scenario seems to be the most probable. At 200 °C the decomposition of $Pd(acac)_2$ occurs quite rapidly, and nucleation may occur both heterogeneously and homogeneously as unsupported Pd NPs are observed 5 min after the $Pd(acac)_2$ injection. Upon

formation, the Pd NPs are not fully stabilized and tend to become attached to iron oxide NPs. This is also confirmed by the complete aggregation of Pd NPs in the absence of iron oxide NPs. However, unlike the sample prepared in the absence of iron oxide NPs, where huge aggregates are formed, in the Pd-5 sample the aggregation is finite and the aggregate size does not exceed 200 nm as is indicated by DLS (Figure S6, SI). But the question arises, why aggregation takes place in these conditions?

NP interactions in solution can be controlled by several, sometimes competing, forces such as van der Waals, electrostatic, magnetic, molecular surface, and depletion effects.[36,37] While electrostatic repulsion/attraction seems to be hardly significant for NPs coated with OA and OAm in a hydrophobic medium, polarization forces might be dominant in solution at the initial stage of aggregation, causing segregation of species of different polarity.[38,39] The Pd dielectric constant was not found in the literature, but for Pt, it is 58 ± 10.[40] The dielectric constant of ferric oxide is 13.1,[41] while for diphenyl ether it is only 3.9.[41] The data for dioctyl ether are not published, but dioctyl phthalate has a dielectric constant of 5.1.[41] Thus, a significant difference in dielectric constants between NPs and the solvent drives polarization forces to cause aggregation of both types of particles, especially at lower reaction temperatures and in a less favorable solvent (diphenyl ether). This scenario is shown in Scheme 1. The other type of forces that should be
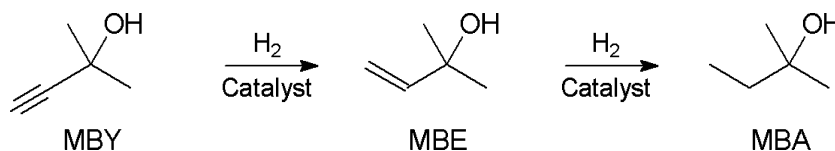
Scheme 1. Schematic Representation of Pd and Iron Oxide NP Aggregation Due to Polarization Forces[a]
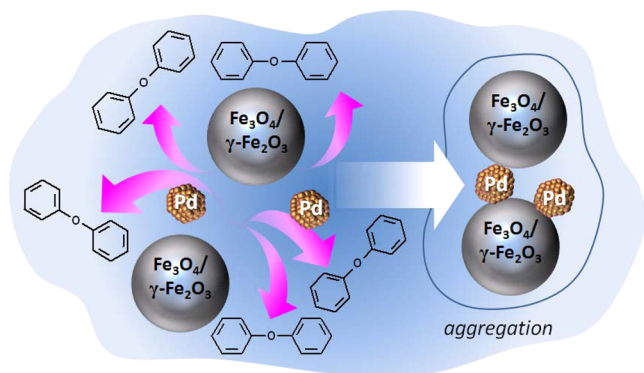
[a]Pink arrows indicate exclusion of the solvent from the interparticle space.

taken into account are magnetic. At the beginning of the iron oxide NP aggregation caused by polarization forces, dipole–dipole interactions change, thus making magnetic forces more important, despite the individual iron oxide NPs being superparamagnetic.[36] In the case of the reaction in dioctyl ether at 285 °C, intensive Brownian motion may prevent aggregation while easier stripping off of surfactant molecules

from the iron oxide NP surface at higher temperatures allows for better stabilization of Pd NPs.

Catalytic Behavior. To test the catalytic activity of the mixtures of Pd and iron oxide NPs and the NP aggregates, the selective hydrogenation of MBY to MBE was studied (Scheme 2).

The data of catalytic testing for representative samples are given in Table 2 and Figure 10. The Pd-1, Pd-2, and Pd-3

Table 2. Results of MBY, MPY, and MNY Hydrogenation Using Pd-Containing Magnetically Separable Catalysts

catalyst notation	Pd, wt %	substrate	selectivity,[b] %	conversion,[c] %	TOF,[d] s^{-1}
Pd-7	87.6	MBY	100	6.2	
Pd-5	24.9	MBY	95.0	95.2	1.9
Pd-4[a] (1st use)	12.6	MBY	96.2	94.9	2.0
Pd-4[a] (2nd use)	12.6	MBY	96.7	95.0	1.8
Pd-4[a] (3rd use)	12.6	MBY	96.6	95.2	1.8
Pd-9	41.6	MBY	96.6	95.0	2.2
Pd-10	28.1	MBY	95.2	93.7	12.3
Pd-7	87.6	MBY	100	6.2	0.1
Pd-4	12.6	MPY	97.9	95.1	2.7
Pd-4	12.6	MNY	96.3	95.2	1.4

[a]After magnetic separation. [b]Selectivity was determined at the conversion indicated in the column to the right. [c]When possible, for a fair comparison of selectivities, the conversion was chosen ~95%. [d]Experimental error in determining TOF is about 10%.
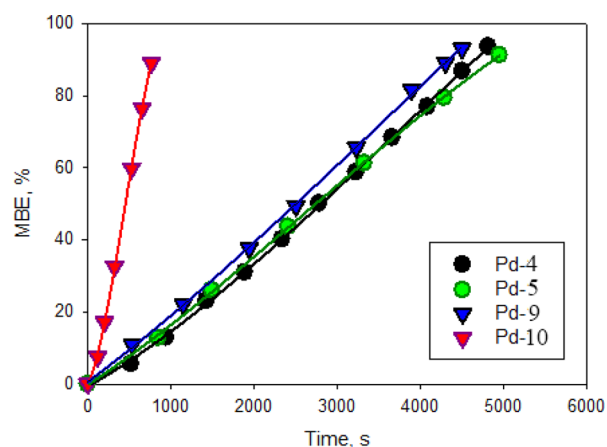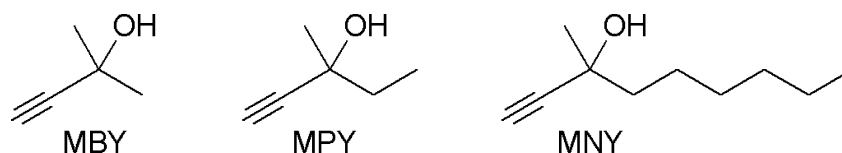

Figure 10. Kinetic curves of MBE accumulation with Pd-4 (black), Pd-5 (green), Pd-9 (blue), and Pd-10 (red).

samples (Table 1) were not considered for catalysis because the NPs are well-dispersed and do not provide efficient magnetic separation. Pd-6 is very similar to Pd-4 and Pd-5. Pd-8 formed too large aggregates and was excluded from consideration.

Scheme 2. Selective Hydrogenation of MBY to MBE[a]

[a]2-Methylbutan-2-ol (MBA) is a side product.

Scheme 3. Formulas of MBY, MPY, and MNY

The Pd-4 and Pd-5 samples based on 8.3 nm Fe_3O_4/γ-Fe_2O_3 NPs demonstrate very similar activities expressed as turnover frequency (TOF), despite Pd-5 forming much larger aggregates than those in the Pd-4 sample (Figure 3). This indicates that the catalytic centers in both catalysts are available for reacting molecules. On the other hand, Pd-4 demonstrates slightly higher selectivity, which even increased upon repeated use (Table 2), while TOF remained nearly unchanged (within an experimental error of ~10%). It is worth noting that, for the repeated use, the catalyst was magnetically separated within 5 min with a negligible catalyst loss. The Pd NPs synthesized without iron oxide NPs (Pd-7) showed only minor activity (Table 2) despite similar Pd NP sizes, which we assign to uncontrolled aggregation in this sample. Thus, the magnetic nanoparticles serve a role beyond simply catalyst separation, following reaction.

The Pd-9 sample based on 22.8 nm Fe_3O_4/γ-Fe_2O_3 NPs shows results (Table 2) analogous to those for Pd-4 and Pd-5, indicating that iron oxide NP size does not influence the catalytic properties. On the other hand, for the Pd-10 sample based on the similar size (22.6 nm) FeO–Fe_3O_4 NPs, the TOF value increases by a factor of 5.6, while selectivity is only slightly lower. This remarkable increase of activity should be assigned to the influence of the iron oxide NP surface. Indeed, the influence of iron oxide NPs on catalytic hydrogenation was demonstrated by us[19] and others[42] for Pt and Au NPs. Even when Pd NPs are not attached to the iron oxide NPs, their close proximity can result in collisions, leading to interactions and electron transfer from the iron oxide NP surface to the Pd surface due to partial reduction, facilitating hydrogenation.[42] Apparently, this influence can be very different depending on the iron oxide structure.

In as-synthesized iron oxide NPs (see Figure 1) prepared by thermal decomposition of iron oleate[22] the major component is FeO, which is combined with Fe_3O_4.[22,23] According to the XPS data, in the Pd-10 sample the iron oxide NPs are additionally oxidized, becoming Fe_3O_4. Preoxidized iron oxide NPs contain Fe_3O_4 and γ-Fe_2O_3 phases and stay unaffected after the Pd NP formation. Thus, our data indicate that lower oxidation state iron species are more efficient in the electron transfer and facilitation of hydrogenation.

With Pd-4 as a catalyst, we also studied the influence of the reacting molecule structure on the selective hydrogenation of different alkyne alcohols. In all of them, the hydroxyl group is adjacent to the triple bond, but the hydrocarbon tail is different. MPY differs from MBY by one CH_2 group, while MNY contains five additional methylene groups. The catalytic tests show that hydrogenation of MPY occurs with a noticeably higher selectivity of almost 98% and slightly faster with TOF = 2.7 s^{-1}. For MNY, both selectivity and activity are the same as those for MBY. These data suggest that there is only a minor dependence of catalytic properties on the alkyne structure, although an improved catalytic performance for MPY is demonstrated. This phenomenon could be explained by a combination of the electron-donating and steric effects. Indeed,

the electron-donating effect of an alkyl chain (the longer the alkyl chain, the stronger the effect) increases the electron density of the alkyne moiety. This would facilitate interaction of the alkyne group with the Pd metal surface, thus facilitating hydrogenation for MPY. However, the longer alkyl chain (the MNY case), would create steric hindrance for the hydrogenation progress, thus offsetting the electron-donating effect.

CONCLUSION

We developed a new method for syntheses of magnetically recoverable catalysts containing both Pd and iron oxide NPs. It is proposed that the controlled aggregation facilitating magnetic recovery is governed by polarization forces combined with magnetic attractions. Such aggregation can be stimulated by lowering the reaction temperature and worsening the solvent affinity toward NPs, but the reaction result also depends on the iron oxide NP size. For 8.3 nm NPs, the aggregation is efficient only in diphenyl ether at both 250 and 200 °C and in dioctyl ether at 200 °C. For much larger (22.8 nm) iron oxide NPs, the aggregation takes place even in dioctyl ether at 285 °C. The catalytic studies of hydrogenation of alkyne alcohols show that all these catalysts are much more active than aggregated Pd NPs prepared under similar reaction conditions but without iron oxide NPs. On the other hand, the major structural parameter influencing the catalytic properties is the composition of iron oxide NPs. The catalyst whose iron oxide NPs contain iron species in a lower oxidation state demonstrate a 5.6-fold increase in TOF, indicating that these species facilitate electron transfer from the iron oxide NP surface to the Pd NP surface.

ASSOCIATED CONTENT

Ⓢ Supporting Information

XPS data, TEM images, and DLS data. This material is available free of charge via the Internet at http://pubs.acs.org.

AUTHOR INFORMATION

Corresponding Author

*E-mail: lybronst@indiana.edu.

Present Address

[⊥]Rosemary Easterday, Department of Chemistry, University of Kentucky, Lexington, Kentucky.

Author Contributions

The manuscript was written through contributions of all authors.

Notes

The authors declare no competing financial interest.

ACKNOWLEDGMENTS

■ **REFERENCES**

(1) Vile, G.; Almora-Barrios, N.; Mitchell, S.; Lopez, N.; Perez-Ramirez, J. From the Lindlar Catalyst to Supported Ligand-Modified Palladium Nanoparticles: Selectivity Patterns and Accessibility Constraints in the Continuous-Flow Three-Phase Hydrogenation of Acetylenic Compounds. *Chem.—Eur. J.* **2014**, *20*, 5926−5937.

(2) Silva, F. P. d.; Rossi, L. M. Palladium on Magnetite: Magnetically Recoverable Catalyst for Selective Hydrogenation of Acetylenic to Olefinic Compounds. *Tetrahedron* **2014**, *70*, 3314−3318.

(3) Long, W.; Brunelli, N. A.; Didas, S. A.; Ping, E. W.; Jones, C. W. Aminopolymer-Silica Composite-Supported Pd Catalysts for Selective Hydrogenation of Alkynes. *ACS Catal.* **2013**, *3*, 1700−1708.

(4) Gao, Y.; Chen, C.-A.; Gau, H.-M.; Bailey, J. A.; Akhadov, E.; Williams, D.; Wang, H.-L. Facile Synthesis of Polyaniline-Supported Pd Nanoparticles and Their Catalytic Properties toward Selective Hydrogenation of Alkynes and Cinnamaldehyde. *Chem. Mater.* **2008**, *20*, 2839−2844.

(5) Lu, A.-H.; Salabas, E. L.; Schueth, F. Magnetic Nanoparticles: Synthesis, Protection, Functionalization, and Application. *Angew. Chim. Int. Ed.* **2007**, *46*, 1222−1244 and references therein.

(6) Chang, B.; Tian, Y.; Shi, W.; Liu, J.; Xi, F.; Dong, X. Magnetically Separable Porous Carbon Nanospheres as Solid Acid Catalysts. *RSC Adv.* **2013**, *3*, 20999−21006.

(7) Dai, Q.; Wang, J.; Yu, J.; Chen, J.; Chen, J. Catalytic Ozonation for the Degradation of Acetylsalicylic Acid in Aqueous Solution by Magnetic CeO2 Nanometer Catalyst Particles. *Appl. Catal., B* **2013**, *144*, 686−693.

(8) Bazgir, A.; Hosseini, G.; Ghahremanzadeh, R. Copper Ferrite Nanoparticles: An Efficient and Reusable Nanocatalyst for a Green One-Pot, Three-Component Synthesis of Spirooxindoles in Water. *ACS Comb. Sci.* **2013**, *15*, 530−534.

(9) Kundu, D.; Chatterjee, T.; Ranu, B. C. Magnetically Separable CuFe2O4 Nanoparticles Catalyzed Ligand-Free C-S Coupling in Water: Access to (E)- and (Z)-Styrenyl-, Heteroaryl and Sterically Hindered Aryl Sulfides. *Adv. Synth. Catal.* **2013**, *355*, 2285−2296.

(10) Wang, D.; Astruc, D. Fast-Growing Field of Magnetically Recyclable Nanocatalysts. *Chem. Rev.* **2014**, *114*, 6949−6985.

(11) Yuzik-Klimova, E. Y.; Kuchkina, N. V.; Sorokina, S. A.; Boris, B.; Morgan, D. G.; Nikoshvili, L. Z.; Lyubimova, N. A.; Matveeva, V. G.; Sulman, E. M.; Stein, B. D.; Svergun, D. I.; Spilotros, A.; Kostopoulou, A.; Lappas, A.; Shifrina, Z. B.; Bronstein, L. M. Magnetically Recoverable Catalysts Based on Polyphenylenepyridyl Dendrons and Dendrimers. *RSC Adv.* **2014**, *4*, 23271−23280.

(12) Wang, Z.; Shen, B.; Zou, A.; He, N. Synthesis of Pd/Fe3O4 Nanoparticle-Based Catalyst for the Cross-Coupling of Acrylic Acid with Iodobenzene. *Chem. Eng. J.* **2005**, *113*, 27−34.

(13) Zhu, Y.; Peng, S. C.; Emi, A.; Su, Z.; Monalisa; Kemp, R. A. Supported Ultra Small Palladium on Magnetic Nanoparticles Used as Catalysts for Suzuki Cross-Coupling and Heck Reactions. *Adv. Synth. Catal.* **2007**, *349*, 1917−1922.

(14) Polshettiwar, V.; Luque, R.; Fihri, A.; Zhu, H.; Bouhrara, M.; Basset, J.-M. Magnetically Recoverable Nanocatalysts. *Chem. Rev.* **2011**, *111*, 3036−3075.

(15) Rossi, L. M.; Silva, F. P.; Vono, L. L. R.; Kiyohara, P. K.; Duarte, E. L.; Itri, R.; Landers, R.; Machado, G. Superparamagnetic Nanoparticle-Supported Palladium: a Highly Stable Magnetically Recoverable and Reusable Catalyst for Hydrogenation Reactions. *Green Chem.* **2007**, *9*, 379−385.

(16) Saha, A.; Leazer, J.; Varma, R. S. O-Allylation of Phenols with Allylic Acetates in Aqueous Media Using a Magnetically Separable Catalytic System. *Green Chem.* **2012**, *14*, 67−71.

(17) Vaddula, B. R.; Saha, A.; Leazer, J.; Varma, R. S. A Simple and Facile Heck-type Arylation of Alkenes with Diaryliodonium Salts Using Magnetically Recoverable Pd-Catalyst. *Green Chem.* **2012**, *14*, 2133−2136.

(18) Sun, W.; Li, Q.; Gao, S.; Shang, J. K. Monometallic Pd/Fe3O4 Catalyst for Denitrification of Water. *Appl. Catal., B* **2012**, *125*, 1−9.

(19) Gumina, G.; Easterday, R.; Malyutin, A. G.; Budgin, A. M.; Stein, B. D.; Nikoshvili, L. Z.; Matveeva, V. G.; Sulman, E. M.; Morgan, D. G.; Bronstein, L. M. γ-Fe2O3 Nanoparticle Surface Controls PtFe Nanoparticle Growth and Catalytic Properties. *Nanoscale* **2013**, *5*, 2921−2927.

(20) Bonrath, W.; Eggersdorfer, M. Catalysis in the Industrial Preparation of Vitamins and Nutraceuticals. *Catal. Today* **2007**, *121*, 45−57.

(21) Park, J.; An, K.; Hwang, Y.; Park, J.-G.; Noh, H.-J.; Kim, J.-Y.; Park, J.-H.; Hwang, N.-M.; Hyeon, T. Ultra-Large-Scale Syntheses of Monodisperse Nanocrystals. *Nat. Mater.* **2004**, *3*, 891−895.

(22) Bronstein, L. M.; Huang, X.; Retrum, J.; Schmucker, A.; Pink, M.; Stein, B. D.; Dragnea, B. Influence of Iron Oleate Complex Structure on Iron Oxide Nanoparticle Formation. *Chem. Mater.* **2007**, *19*, 3624−3632.

(23) Bronstein, L. M.; Atkinson, J. E.; Malyutin, A. G.; Kidwai, F.; Stein, B. D.; Morgan, D. G.; Perry, J. M.; Karty, J. A. Nanoparticles by Decomposition of Long Chain Iron Carboxylates: From Spheres to Stars and Cubes. *Langmuir* **2011**, *27*, 3044−3050.

(24) Easterday, R.; Sanchez-Felix, O.; Stein, B. D.; Morgan, D. G.; Maren, P.; Losovyj, Y.; Bronstein, L. M. Structural Study of Pt-Fe Nanoparticles: New Insights into Pt Bimetallic Nanoparticle Formation with Oxidized Fe Species. *J. Phys. Chem. C* **2014**, *118*, 24769−24775.

(25) Zhu, Y.; Jiang, F. Y.; Chen, K.; Kang, F.; Tang, Z. K. Size-Controlled Synthesis of Monodisperse Superparamagnetic Iron Oxide Nanoparticles. *J. Alloys Compd.* **2011**, *509*, 8549−8553.

(26) Shi, W.; Zhu, J.; Sim, D. H.; Tay, Y. Y.; Lu, Z.; Zhang, X.; Sharma, Y.; Srinivasan, M.; Zhang, H.; Hng, H. H.; Yan, Q. Achieving High Specific Charge Capacitances in Fe3O4/Reduced Graphene Oxide Nanocomposites. *J. Mater. Chem.* **2011**, *21*, 3422−3427.

(27) Metin, O.; Duman, S.; Dinc, M.; Ozkar, S. Oleylamine-Stabilized Palladium(0) Nanoclusters As Highly Active Heterogeneous Catalyst for the Dehydrogenation of Ammonia Borane. *J. Phys. Chem. C* **2011**, *115*, 10736−10743.

(28) Hawn, D. D.; DeKoven, B. M. Deconvolution as a Correction for Photoelectron Inelastic Energy Losses in the Core Level XPS Spectra of Iron Oxides. *Surf. Interface Anal.* **1987**, *10*, 63−74.

(29) Muhler, M.; Schoegl, R.; Ertl, G. The Nature of the Iron Oxide-Based Catalyst for Dehydrogenation of Ethylbenzene to Styrene. 2. Surface Chemistry of the Active Phase. *J. Catal.* **1992**, *138*, 413−444.

(30) Yamashita, T.; Hayes, P. Analysis of XPS Spectra of Fe2+ and Fe3+ Ions in Oxide Materials. *Appl. Surf. Sci.* **2008**, *254*, 2441−2449.

(31) Santra, S.; Ranjan, P.; Bera, P.; Ghosh, P.; Mandal, S. K. Anchored Palladium Nanoparticles onto Single Walled Carbon Nanotubes: Efficient Recyclable Catalyst for N-Containing Heterocycles. *RSC Adv.* **2012**, *2*, 7523−7533.

(32) Karimi, B.; Behzadnia, H.; Bostina, M.; Vali, H. A Nano-Fibrillated Mesoporous Carbon as an Effective Support for Palladium Nanoparticles in the Aerobic Oxidation of Alcohols "on Pure Water". *Chem.—Eur. J.* **2012**, *18*, S8634/8631−S8634/8624.

(33) Moulder, J. F.; Stickle, W. F.; Sobol, P. E.; Bomben, K. D. *Handbook of X-ray Photoelectron Spectroscopy, Physical Electronics*; Physical Electronics: Eden Prairie, MN, 1995; p 261.

(34) Cornell, R. M.; Schwertmann, U. *The Iron Oxides*; VCH: New York, 1996.

(35) Guo, J.; Gu, H.; Wei, H.; Zhang, Q.; Haldolaarachchige, N.; Li, Y. Y.; P, D.; Wei, S.; Guo, Z. Magnetite-Polypyrrole Metacomposites: Dielectric Properties and Magnetoresistance Behavior. *J. Phys. Chem. C* **2013**, *117*, 10191−10202.

(36) Bishop, K. J. M.; Wilmer, C. E.; Soh, S.; Grzybowski, B. A. Nanoscale Forces and their Uses in Self-Assembly. *Small* **2009**, *5*, 1600−1630.

(37) Ye, X.; Millan, J. A.; Engel, M.; Chen, J.; Diroll, B. T.; Glotzer, S. C.; Murray, C. B. Shape Alloys of Nanorods and Nanospheres from Self-Assembly. *Nano Lett.* **2013**, *13*, 4980−4988.

(38) Gomila, G.; Esteban-Ferrer, D.; Fumagalli, L. Quantification of the Dielectric Constant of Single Non-Spherical Nanoparticles from Polarization Forces: Eccentricity Effects. *Nanotechnology* **2013**, *24*, 505713/505711−505713/505718.

(39) Israelachvili, J. N. *Intermolecular and Surface Forces*, Third ed.; Academic Press: Waltham, MA, 2011; p 709.

(40) Choi, W. S.; Seo, S. S. A.; Kim, K. W.; Noh, T. W.; Kim, M. Y.; Shin, S. Dielectric Constants of Ir, Ru, Pt, and IrO2. Contributions from Bound Charges. *Phys. Rev. B* **2006**, *74*, 205117/205111−205117/205118.

(41) http://deltacnt.com/99-00032.htm. (Accessed August 15, 2014).

(42) Milone, C.; Crisafulli, C.; Ingoglia, R.; Schipilliti, L.; Galvagno, S. A Comparative Study on the Selective Hydrogenation of Alpha, Beta Unsaturated Aldehyde and Ketone to Unsaturated Alcohols on Au Supported Catalysts. *Catal. Today* **2007**, *122*, 341−351.